Geophysical Journal International

Geophys. J. Int. (2015) **202,** 1566–1580 doi: 10.1093/gji/ggv225
GJI Seismology

Off-fault shear failure potential enhanced by high-stiff/low-permeable damage zone during fluid injection in porous reservoirs

J. Rohmer,[1] T.K. Nguyen[1] and A. Torabi[2]

[1]*BRGM, 3 av. C. Guillemin - F-45060 Orléans Cédex 2, France. E-mail: j.rohmer@brgm.fr*
[2]*Uni Research CIPR, P.O. Box 7810, 5020 Bergen, Norway*

Accepted 2015 May 28. Received 2015 May 28; in original form 2014 December 12

SUMMARY

Several studies have focused on the role of damage zone (DZ) on the hydromechanical behaviour of faults by assuming a fractured DZ (i.e. low stiffness/high permeability). Yet, this vision may not be valid in all geological settings, in particular, in high-porosity reservoirs as targeted by several underground exploitations. We investigate the impact of a high-stiff/low-permeable DZ on the shear reactivation of a blind, undetectable normal fault (1 km long, $\leq$10 m offset), with a 0.5 m thick low-porosity/permeability fault core during fluid injection into a high-porosity reservoir. The spatial distribution of effective properties (elastic moduli, Biot's coefficients and permeability) of DZ including deformation bands (DB; elliptic inclusions) and intact rock were derived using upscaling analytical expressions. The influence of DZ on the hydromechanical behaviour of the fault zone was numerically explored using 2-D plane-strain finite-element simulations within the framework of fully saturated isothermal porous media by accounting for an orthotropic elastic rheology. The numerical results showed that the presence of DB plays a protective role by reducing the potential for shear reactivation inside the fault core. On the other hand, they favour shear failure in the vicinity of the fault core (off-fault damage) by accelerating the decrease of the minimum principal effective stress while limiting the decrease of the maximum one. This behaviour is strongly enhanced by the fault-parallel DZ effective stiffness, but limited by the combined effect of fault-normal DZ effective permeability and of the Biot's coefficients. This can have implications for the location and size of aftershocks during fault reactivation.

Key words: Numerical approximations and analysis; Geomechanics; Microstructures; Fracture and flow; Fault zone rheology.

1 INTRODUCTION

Reactivation of faults during fluid injection into porous reservoirs is a major concern, either because they might potentially cause fractures, which act as pathways of leakage (Zoback & Gorelick 2012) and induce earthquakes (Ellsworth 2013). The importance of hydromechanical processes in the initiation and dynamic slip propagation (earthquakes) has received considerable attention over the last decade (e.g. Faulkner *et al.* 2010). In general, the role of fault structure on dynamic rupturing was studied by, for example, Rudnicki & Rice 2006; Dunham & Rice 2008; Viesca *et al.* 2008, who highlighted more specifically, the importance of spatial distribution of properties (heterogeneities) on either sides of faults (off-fault zones). Based on extensive outcrop studies, a fault includes a 'damage zone (DZ) and a fault core (FC)' as the main structural elements. This architecture can be found at different spatial scales in all kinds of lithologies, whether in siliciclastic or in carbonate geological settings (Caine *et al.* 1996; Faulkner *et al.* 2010; Kolyukhin & Torabi 2012; Wibberley *et al.* 2008).

The FC is where the main slip surface is located and hence where the most fault throw is accommodated. It is characterised by the presence of highly deformed and weathered material such as granular gouge composed of broken clasts, clay gouge, clay smear, breccia zone and diagenetic features (e.g. Wibberley *et al.* 2008). This heterogeneous texture within the FC affects its coefficient of friction (ranging between 0.4 and 0.6), depending on the clay content (e.g. Shimamoto & Logan 1981). In addition, this will hamper the petrophysical properties of FC such as capillary threshold pressure and the flow conductivity (e.g. Yielding *et al.* 1997; Manzocchi *et al.* 2010). The FC is generally surrounded by a DZ that may either act as a conduit (in fractured DZ) or a barrier to flow (in DZ, where deformation bands or veins (mineral-filled fractures) are dominant) depending on the characteristics of the deformations features and initial host rock properties. Fig. 1 schematically depicts three main conceptual models of fault based on the hydraulic behaviour of FC and DZ following the classification proposed by Caine *et al.* (1996).

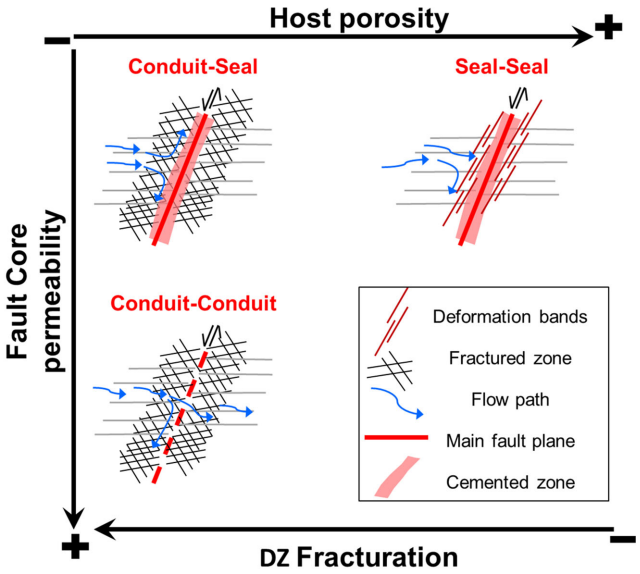

Figure 1. Classification of the main conceptual models for fault zone's representation depending on the host rock porosity, the damage zone DZ fracturation and the FC's permeability (adapted from Matonti *et al.* 2012). The model concept of 'seal–seal' is at the core of the present study.

A first concept referred to as 'conduit-seal' assumes a low-permeability/porosity core acting as a barrier to flow and a DZ made of dilatant fractures, hence acting as a drain or conduit. The degree of fracturing generally increases toward the FC (Fig. 1), which corresponds to reduction in the Young's modulus and permeability increase in the DZ close to the FC (e.g. Faulkner *et al.* 2006). Such heterogeneities have been demonstrated to play a significant role in the shear reactivation and dynamic rupture rupturing of the fault during fluid injection (Guglielmi *et al.* 2008; Cappa 2011; Jeanne *et al.* 2013, 2014; Rohmer 2014). The second concept 'conduit-conduit' in Fig. 1 assumes a fractured DZ with fractured and poorly cemented core (see an example in carbonates presented by Matonti *et al.* 2012) so that this fault acts as a complete drain to flow. Yet, the vision of a fractured DZ cannot be applied to all types of rocks, because the deformation mechanisms can take various forms in high-porosity rock formations as targeted by several underground exploitations (like wastewater disposal, seasonal natural gas storage, CO_2 geological storage, etc.). A third concept referred to as 'seal-seal' in Fig. 1 assumes a sealing core with a DZ acting as a barrier to flow. The sealing capacity of DZ strongly depends on the characteristics of deformation features inside it. In low-porosity setting like carbonate reservoirs, this can be related to the presence of mineral-filled fractures/veins or stylolites due to dissolution processes (Tondi *et al.* 2006), whereas in high-porosity reservoirs, this can be related to low-permeability/high-stiff deformation bands, DB (Fisher & Knipe 2001; Fossen *et al.* 2007) which generally tend to be subparallel to the main fault plane (e.g. Shipton & Cowie 2001). In the present study, we focus on this latter case.

Deformation bands can be classified by deformation mechanisms (Fossen *et al.* 2007), which determine in turn their hydraulic and mechanical (elastic and failure parameters) properties. These correspond to (1) disaggregation of grains via grain boundary sliding and reorganization and, grain cement breaking or granular flow with little to no influence on porosity; (2) cataclasis involving grain abrasion and fracturing to different degrees, which commonly reduces porosity; (3) phyllosilicate smearing, where clay minerals are abundant and make barriers to flow along the bands; (4) dissolution and cementation, which are mostly post-deformation and would have additional impact on the band porosity. Kinematically, deformation bands could be classified in three end members: dilation, compaction and shear bands or a combination of them depending on the stress state responsible for their formations (Alikarami *et al.* 2013). In the present study, we are interested in injection of fluid into a DZ, which encompasses both lower porosity and permeability and higher stiffness than its host rock. This is in contrary to the situation, where the fluid is injected into low-porosity rocks, where deformation features usually take the form of fractures with high permeability and low stiffness (Torabi & Zarifi 2014). Thus, we primarily focus on cataclastic bands with both compaction and shear components (compaction shear bands) formed in the DZ of a normal fault bounding a reservoir between a low-permeable caprock and underburden formation (see Fig. 2, corresponding to a critical geometrical case for fault activation during fluid injection, e.g. Hawkes *et al.* 2004). These bands are referred to as deformation bands and denoted DB in the following.

Commonly, DB exhibits a reduction in permeability of two to three, and locally as much as six, orders of magnitude with respect to the host rock. On the other hand, Young's modulus could be higher than the adjacent host rocks (Jourde *et al.* 2002; Schultz & Siddharthan 2005; Fossen *et al.* 2007; Alikarami *et al.* 2013). Regarding failure parameters, existing data outline that DB are stronger than their host rock (e.g. Mair *et al.* 2000), which is attributed to an increase of the bulk uniaxial compressive strength in the band (see e.g. Torabi & Alikarami 2012). The amount of strengthening depends on several factors related to shear-driven cataclasis or density of grain packing or the degree of late cementation (e.g. Underhill & Woodcock 1987; Kaproth *et al.* 2010; Petrie *et al.* 2014). While coefficient of friction is usually increased (Kaproth *et al.* 2010; Petrie *et al.* 2014), cohesive strength can either be maintained or increased as stated by Fossen *et al.* (2007).

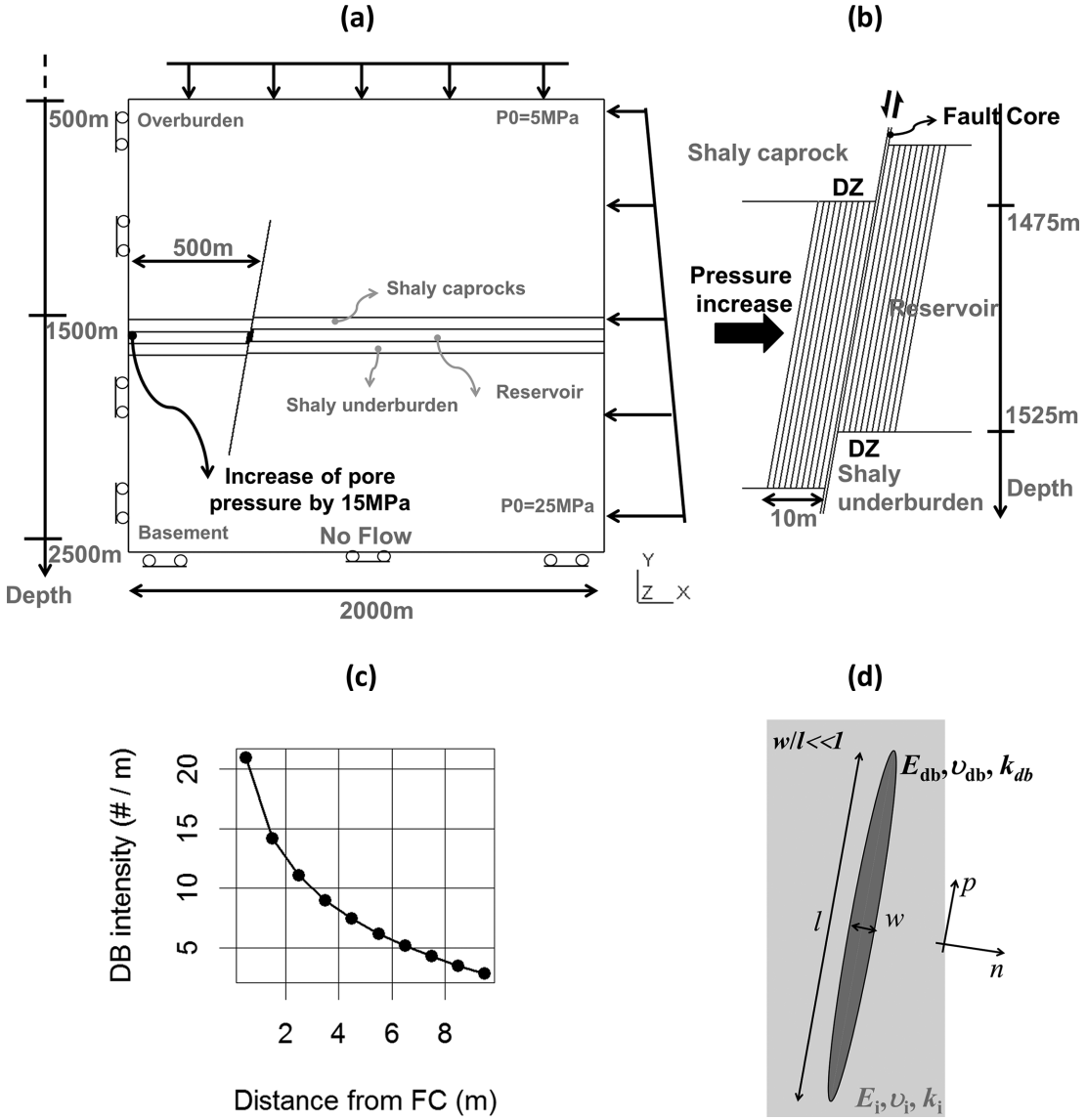

Figure 2. (a) Model geometry and boundary conditions; (b) discretization of the damage zone DZ into 1-m-thick parallel zones; (c) deformation bands' density assigned to each DZ (number of DB per metre) as a function of the lateral distance to the fault core FC; (d) schematic overview of an elongated (length $l \gg$ width w) DB embedded within the intact reservoir rock. Fault-parallel direction is indicated by 'p', whereas the fault-normal one is indicated by 'n'.

Previous studies have shown that the decrease of stiffness due to open fractures within DZ in a conduit-seal model (Fig. 1), can promote fault slip during pore pressure increase (i.e. a fault weakening or strain softening), see in particular (Faulkner *et al.* 2006). In the present study, we question whether the impact of the DB in high-porosity sandstones can have a reverse effect, that is, potentially leading to a 'fault strengthening or strain hardening'. In this view, we use numerical simulations, which are described in Section 2. Instead of assuming a generic relationship for the evolution of the hydromechanical properties of DZ with the distance to FC (like in Cappa 2011 or Rohmer 2014), we use a combination of statistical analysis of field data (Schueller *et al.* 2013) and upscaling techniques to derive the effective DZ properties (Section 3). In Section 4, the numerical simulations showed that the maximum shear reactivation is located in the DZ compartment adjacent to the FC. We investigate the significance of changing DB properties (elastic moduli, Biot's coefficients, and permeability) on the behaviour of fault and DZ. Then, a systematic parametric study is conducted on permeability, on Young's modulus, and on the Biot's coefficient to discover the effect of material properties in DZ on the behaviour of the fault.

2 METHODS

In this section, we first describe the assumptions underlying the model set-up (Section 2.1) and then provide the details of the upscaling techniques used to account for the presence of high-stiff/low-permeable DB within the DZ (Section 2.2).

Table 1. Properties of rock formations (properties of DZ are detailed in Section 3.1).

Property	Unit	Overburden	Caprock & underburden	Reservoir (host rock)	Basement	Core
Young's modulus	GPa	15	5	15	35	1
Poisson's ratio	–	0.30	0.25	0.25	0.30	0.30
Intrinsic Permeability	m^2	10^{-13}	10^{-19}	10^{-13}	10^{-16}	10^{-17}
Porosity	%	15	1	15	15	1
Biot's coefficient	–	1.0	1.0	1.0	1.0	1.0

2.1 Model setup

For most underground exploitations, major faults can be detected and therefore avoided through careful selection of the site. However, a major concern remains the potential for induced seismicity due to undetectable small faults with shear displacement $D \leq 10$ m, which are below seismic resolution. As shown by Mazzoldi *et al.* (2012), such fault systems should be capable of generating sufficiently large events that could be felt at the surface with magnitude up to 3.0. Therefore, we focus on this worst case by representing a normal 1000-m-long blind fault with a dip angle of 80° and $D = 10$ m in a 2-D plane-strain finite-element model (2000 m × 2000 m) composed of a highly permeable porous reservoir formation (with thickness $H = 50$ m) bounded at the top and bottom by low-permeable 50-m-thick caprock formations. The setting of 1500-m-deep porous reservoir is similar to the one described by Rohmer (2014), see Fig. 2(a). We assume an initial hydrostatic fluid pressure, a vertical stress gradient of 2.217×10^4 Pa m^{-1}, a bulk density of 2260 kg m^{-3}. We focus on an extensional stress regime, since it was identified as a critical case for fault reactivation during fluid injection (e.g. Hawkes *et al.* 2004). An initial stress state is defined as follows $\sigma_H = K_0 \times \sigma_V$, with $K_0 = 0.70$. The properties of the different rock formations (except for DZ) are summarized in Table 1. In particular, we assume a worst case scenario for the FC by representing it as a 0.5-m-thick low-porosity medium with low permeability of 10^{-17} m^2 and porosity of 1 per cent, with a low Young's modulus of 1 GPa (using the lower bound as reported by Cappa & Rutqvist 2011).

The injection of fluid is modelled by imposing an over-pressure (difference between the final and initial pore pressure) at the lateral left boundary of the reservoir (Fig. 2a). This is linearly increased during ∼100 days by the step of ≈10 days from 0 to a maximum value of 15 MPa, that is, about 100 per cent of the initial pore pressure: this value is an extreme case for shear reactivation (injection is typically designed by setting a maximum over-pressure value ranging from 30 to ∼80 per cent of the initial pore pressure as reported for real cases in USEPA, 1994). Since we use a plane strain model, the modelled injection scenario corresponds to fluid injection through a horizontal wellbore.

In the present study, we focus on initiation of shear reactivation (and not rupture processes), that is, on the likelihood of failure initiation. For this purpose, the problem is solved within the framework of fully saturated isothermal porous elastic media using the finite element code Code_Aster. Further details on the governing equations of the poro-elastic model are provided in the Appendix (details on the numerical implementation can be found in EdF R&D 2012).

Following the approach of Cappa (2011), the DZ is discretized by multiple, 1-m-thick parallel zones characterized by hydromechanical properties reflecting the heterogeneity of DB density (Fig. 1b). The DZ width W is defined based on the statistical analysis of Schueller *et al.* (2013) by using the distance from the FC to the point at which the average frequency of deformation bands is 5 m^{-1}. This is related to the fault throw (here of 10 m) through a power law function so that $W = 2.32 \times 10^{0.46} \approx 6.70$ m. In the model, the DZ width is assumed to be larger (here 10 m) to account for average frequency of deformation bands (see rightmost part of the DB density in Fig. 2c).

Effective properties of DZ depending on the DB density are further described in Section 2.2. Since the presence of DB introduces anisotropy in the spatial distribution of the DZ properties, we use the generalized law of effective stress incorporating anisotropic poro-elasticity (e.g. Carroll 1979; Chen & Nur 1992):

$$\sigma'_{ij} = \sigma_{ij} - \beta_{ij} P_f, \tag{1}$$

where $\boldsymbol{\sigma}$ is the total stress tensor, P_f is the pore pressure and $\boldsymbol{\sigma}'$ is the effective stress tensor and $\boldsymbol{\beta}$ is the second-rank Biot tensor (Biot 1941), which controls the magnitude and direction of the pore-pressure/stress coupling and is defined as follows:

$$\beta_{ij} = \delta_{ij} - c_{ijkl} s'_{klmm}, \tag{2}$$

where δ is the Kronecker delta, $\boldsymbol{c}$ is the elastic stiffness of the rock composed of intact porous matrix and deformation bands and $\boldsymbol{s}'$ is the elastic compliance of the intact rock (Carroll 1979).

In the present study, we are interested in shear reactivation not only along the main fault plane (represented by a FC of 0.5 m thick), but also within the DZ. We use the Mohr–Coulomb theory by the Coulomb Failure Criterion (CFC; Jaeger & Cook 1979) defined as the following:

$$\mathrm{CFC} = \left[\frac{\sigma'_1 - \sigma'_3}{2}\right]\sqrt{(1+\mu^2)} - \mu\left[\frac{\sigma'_1 + \sigma'_3}{2}\right] - C_0, \tag{3}$$

where σ'_1 and σ'_3 are respectively the maximum and the minimum effective principal stresses (compressive stresses are assumed to be positive), μ is the coefficient of internal friction and C_0 is the cohesion. To assess the tendency for shear failure, we then define the potential for shear failure 'PSF' as the distance $\sigma'_1 - (\sqrt{(1+\mu^2)} + \mu)/(\sqrt{(1+\mu^2)} - \mu)\sigma'_3$ to the cohesive threshold at $\hat{C}_0 = 2C_0/(\sqrt{(1+\mu^2)} - \mu)$. Assuming

$\mu = 0.6$, PSF can be formulated as $\sigma_1' - 3\sigma_3'$ with threshold $\hat{C}_0 \approx 3.5C_0$. It should be underlined that this criterion is primarily used to identify the locations where shear reactivation is promoted (with PSF $> \hat{C}_0$) or limited (with PSF $\leq \hat{C}_0$) relative to a fault system with or without DZ.

2.2 Upscaling methods

The DZ material is viewed as a two-phase material composed of the intact rock matrix and of the DB considered as elliptic inclusions (see a schematic overview in Fig. 2d). The effective hydromechanical properties (permeability, elastic moduli and Biot's coefficients) of such a composite porous medium depend on the number of DB, their geometry (aspect ratio, i.e. width to length ratio and orientation) and their properties.

The density of DB (d) in the DZ of faults (number of DB per meter) has been extensively addressed in the literature (see Schueller *et al.* 2013 and references therein). Considering a throw of 10 m, we use the relationship derived by Schueller *et al.* (2013) so that:

$$d(x) = A + L \times \log(x), \tag{4}$$

where x is the distance to the FC, the empirical parameters $A \approx 16.67$ and $L \approx -6.14$ are related to the DZ width W and to the spatial mean of DB density inside DZ [i.e. average value over space, which is here assumed to be constant at 12 deformation bands per meter, see further details in Schueller *et al.* (2013): section 5]. The relationship described by eq. (4) is depicted in Fig. 2(c).

Deformation bands in DZs generally tend to be subparallel to the main fault plane (e.g. Shipton & Cowie 2001) with very small thickness (millimetre to centimetre scale): the elliptic inclusions are thus considered monotonically aligned along the fault plane (fault parallel) and thin, that is, with cross-sections in the limit case of aspect ratio approaching zero (laminated case). In the following, we assume a low inclusion's aspect ratio of 10^{-4} (e.g. thickness of 0.5 mm and length of 5 m).

Based on the afore-described assumptions, we apply the techniques for estimating the effective elastic properties of composites reinforced by monotonically aligned fibres (ribbons) provided by Zhao & Weng (1990) using the Eshelby–Mori–Tanaka theory. The expressions for the orthotropic elastic moduli, that is, co-planar to the elliptic cross-sections, with subscript 'p' indicating along the major ellipsoid axis (fault-parallel direction) and subscript 'n' indicating perpendicular to it (fault-normal direction), as depicted in Fig. 2(d), are as follows:

$$E_\mathrm{p} = f_\mathrm{db}E_\mathrm{db} + f_\mathrm{i}E_\mathrm{i} + \frac{4f_\mathrm{db}f_\mathrm{i}(\upsilon_\mathrm{db} - \upsilon_\mathrm{i})^2}{f_\mathrm{db}(1/K_\mathrm{i} + 1/G_\mathrm{i}) + f_\mathrm{i}(1/K_\mathrm{db} + 1/G_\mathrm{db})} \tag{5a}$$

$$E_\mathrm{n} = \frac{f_\mathrm{db}E_\mathrm{db}K_\mathrm{db}(K_\mathrm{i} + G_\mathrm{i}) + f_\mathrm{i}E_\mathrm{i}K_\mathrm{i}(K_\mathrm{db} + G_\mathrm{db})}{f_\mathrm{db}f_\mathrm{i}(G_\mathrm{db} - G_\mathrm{i})(3(K_\mathrm{db} - K_\mathrm{i}) - (G_\mathrm{db} - G_\mathrm{i})) + f_\mathrm{db}K_\mathrm{db}G_\mathrm{i} + f_\mathrm{i}K_\mathrm{i}G_\mathrm{db} + K_\mathrm{db}K_\mathrm{i}} \tag{5b}$$

$$G_\mathrm{np} = f_\mathrm{db}/G_\mathrm{db} + f_\mathrm{i}/G_\mathrm{i} \tag{5c}$$

$$\upsilon_\mathrm{np} = f_\mathrm{db}\upsilon_\mathrm{db} + f_\mathrm{i}\upsilon_\mathrm{i} + \frac{f_\mathrm{db}f_\mathrm{i}(\upsilon_\mathrm{db} - \upsilon_\mathrm{i})(\upsilon_\mathrm{db}G_\mathrm{i} - \upsilon_\mathrm{i}G_\mathrm{db})}{f_\mathrm{db}G_\mathrm{db}(1 - \upsilon_\mathrm{i}) + f_\mathrm{i}G_\mathrm{i}(1 - \upsilon_\mathrm{db})}, \tag{5d}$$

where the subscript 'i' and 'db' respectively designates the properties of the intact rock matrix and the ones of the inclusion (DB); E is the Young's modulus; υ is the Poisson's ratio; K and G are the bulk and the shear elastic moduli; f is the volume fraction of the respective phase ($f_\mathrm{i} = 1 - f_\mathrm{db}$). The properties of the intact rock are: $E_\mathrm{i} = 15$ GPa, $\upsilon_\mathrm{i} = 0.25$, $K_\mathrm{i} = 10$ GPa and $G_\mathrm{i} = 6$ GPa. The properties of the inclusion are derived from the ones of the intact rocks by assuming the value of the Young's modulus contrast $E_\mathrm{db}/E_\mathrm{i}$ and $\upsilon_\mathrm{db} = 0.20$.

The Biot's tensor is then evaluated using Eq. (2) and the stiffness tensor and elastic compliance tensor derived from the afore-described effective properties by further assuming that the intact rock matrix of the DZ is isotropic with homogeneous properties (see also the Appendix).

For the hydraulic part, we assume that the DZ can be assimilated to a laminated medium (in the limit case of elongated inclusions) so that the effective hydraulic conductivity k is derived by using the Voigt-Reuss bounds (e.g. Markov 1999)

$$k_\mathrm{p} = f_\mathrm{db}k_\mathrm{db} + f_\mathrm{i}k_\mathrm{i} \tag{6a}$$

$$k_\mathrm{n} = \left(f_\mathrm{db}k_\mathrm{db}^{-1} + f_\mathrm{i}k_\mathrm{i}^{-1}\right)^{-1}. \tag{6b}$$

The intrinsic permeability of the inclusion k_db is derived by assuming a value of the permeability contrast $k_\mathrm{i}/k_\mathrm{db}$ with $k_\mathrm{i} = 10^{-13}$ m^2.

Using the DB density as depicted in Fig. 2(c), the spatial distribution of the orthotropic effective DZ pore-elastic and hydraulic properties are computed as a function of lateral distance to FC. At a given lateral distance x from the FC, the DB volume fraction f_db is related to its density $d(x)$ (eq. 4) and to the ratio of elliptic inclusions' volume ($l \times w \times \pi$) along the whole reservoir thickness ($H = 50$ m) to the total volume of the 1-m-thick compartment as follows:

$$f_\mathrm{db}(x) = \frac{H \times d(x) \times l \times w \times \pi}{H \times 1} = d(x) \times l \times w \times \pi. \tag{7}$$

3 RESULTS

In this section, we first derive the upscaled DZ properties by considering different scenarios for $E_\mathrm{db}/E_\mathrm{i}$ and $k_\mathrm{i}/k_\mathrm{db}$ (Section 3.1). Then, the hydromechanical behaviour of the fault zone during fluid injection is compared between a case neglecting the DZ presence, that is, DZ has

Table 2. Simulation cases considering different DZ properties (SC: spatially constant; SV: spatially varying). Bold values correspond to the values modified compared to case 1.

Case	Young's modulus		Biot's coefficient		Permeability	
	E_n	E_p	β_n	β_p	k_n	k_p
0	SC: 15 GPa	SC: 15 GPa	SC: 1.0	SC: 1.0	SC: 10^{-13} m^2	SC: 10^{-13} m^2
1	SV: $E_{db}/E_i = 2.40$	SV: $E_{db}/E_i = 2.40$	SV: $E_{db}/E_i = 2.40$	SV: $E_{db}/E_i = 2.40$	SV: $k_i/k_{db} = 4450$	SV: $k_i/k_{db} = 4450$
2	**SC: 15 GPa**	SV: $E_{db}/E_i = 2.40$	SV: $E_{db}/E_i = 2.40$	SV: $E_{db}/E_i = 2.40$	SV: $k_i/k_{db} = 4450$	SV: $k_i/k_{db} = 4450$
3	SV: $E_{db}/E_i = 2.40$	**SC: 15 GPa**	SV: $E_{db}/E_i = 2.40$	SV: $E_{db}/E_i = 2.40$	SV: $k_i/k_{db} = 4450$	SV: $k_i/k_{db} = 4450$
4	SV: $E_{db}/E_i = 2.40$	SV: $E_{db}/E_i = 2.40$	**SC: 1.0**	SV: $E_{db}/E_i = 2.40$	SV: $k_i/k_{db} = 4450$	SV: $k_i/k_{db} = 4450$
5	SV: $E_{db}/E_i = 2.40$	SV: $E_{db}/E_i = 2.40$	SV: $E_{db}/E_i = 2.40$	**SC: 1.0**	SV: $k_i/k_{db} = 4450$	SV: $k_i/k_{db} = 4450$
6	SV: $E_{db}/E_i = 2.40$	SV: $E_{db}/E_i = 2.40$	SV: $E_{db}/E_i = 2.40$	SV: $E_{db}/E_i = 2.40$	**SC: 10^{-13} m^2**	SV: $k_i/k_{db} = 4450$
7	SV: $E_{db}/E_i = 2.40$	SV: $E_{db}/E_i = 2.40$	SV: $E_{db}/E_i = 2.40$	SV: $E_{db}/E_i = 2.40$	SV: $k_i/k_{db} = 4450$	**SC: 10^{-17} m^2**
8	SV: $E_{db}/E_i = 1.75$	SV: $E_{db}/E_i = 1.75$	SV: $E_{db}/E_i = 1.75$	SV: $E_{db}/E_i = 1.75$	SV: $k_i/k_{db} = 7780$	SV: $k_i/k_{db} = 7780$
9	SV: $E_{db}/E_i = 3.35$	SV: $E_{db}/E_i = 3.35$	SV: $E_{db}/E_i = 3.35$	SV: $E_{db}/E_i = 3.35$	SV: $k_i/k_{db} = 2230$	SV: $k_i/k_{db} = 2230$

the properties of the intact reservoir rock (case 0) and a case with spatially varying orthotropic DZ properties (case 1) assuming $E_{db}/E_i = 2.40$ and $k_i/k_{db} = 4450$ (Section 3.2). On this basis, a parametric study is carried out to identify the property, which has significant effect on the hydromechanical behaviour of the fault (Section 3.3). Finally, the combined role of permeability and stiffness contrast is explored (Section 3.4). Table 2 summarises the different simulation cases investigated in this section.

3.1 Upscaled DZ properties

We first derive the effective (upscaled) DZ properties (Young's modulus and Biot's coefficients) considering different scenarios of Young's modulus contrast E_{db}/E_i (varying from 1.40 to 3.35) as depicted in Fig. 3. We show that the shear behaviour of the near-fault (shorter distance from FC) is pronouncedly influenced by the presence of DB due to the power-law decay of the DB density (Fig. 2c). The fault-parallel (denoted E_p) Young's modulus appears to be larger than E_i (with values up to >2.5, Fig. 3b), and larger than the fault-normal one (denoted E_n in Fig. 3a): compare, for instance, red-coloured curves the largest contrast E_{db}/E_i in Figs 3(a) and (b). This behaviour is in agreement with the reinforcement role of inclusion along their major axis. The Biot's coefficients decrease near the FC, which are inferred to have a negative correlation with the Young's moduli (Figs 3c and d). The fault-parallel Biot's coefficient β_p is the one decreasing the most and reaches values below 0.60 in the fault near-zone for the case with the largest contrast E_{db}/E_i (Fig. 3d).

Fig. 4 depicts the evolution of the upscaled permeability considering now different permeability's contrast k_i/k_{db} (varying from 1120 to 7780). We show that the presence of DB largely influences the fault-normal permeability (denoted k_n) with a decrease of up to four orders of magnitude compared to k_i. Conversely, the fault-parallel permeability (denoted k_p) is little impacted by k_i/k_{db} (only a single case is shown for sake of clarity in Fig. 3c, bottom) with a moderate decrease of up to one order of magnitude compared to k_{db}. This is related to the assumption of a single fault-parallel DB family.

3.2 Analysis of the global behaviour

We first analyse the hydromechanical behaviour of the fault system for case 0, that is, neglecting DZ. Due to the reservoir high permeability (10^{-13} m^2), the lateral spreading of pore pressure P_f rapidly reaches the regions of the fault. Fig. 5(a, top) shows the spatial distribution of P_f after 100 days of injection: P_f is almost constant at ~30 MPa (corresponding to the final injection pressure) within the hanging-wall reservoir compartment, whereas P_f is lower (~20 MPa) within the foot-wall compartment, since the FC low-permeability (of 1e^{-17} m^2) material limits the lateral fluid flow. It should also be noted that P_f increases in the shaly underburden formation directly adjacent to the hanging-wall reservoir compartment, but the penetration of this over-pressure remains limited due to the underburden's low permeability (of 1e^{-19} m^2). The increase of P_f induces the reduction in both effective stress components $(\sigma_3'; \sigma_1')$ as shown on the lateral profiles at −1515-m-depth in Fig. 6 (case 0 in black), so that the shear failure criterion ($\mu = 0.6$ and $C_0 = 0$) can be reached at the end of injection. Fig. 5(a, bottom) highlights that the weakest location (maximum value of PSF > 0) is located at the reservoir bottom (over depths' range from −1515 to −1520 m). In the following, we focus on the analysis of this location.

Let us now consider case 1 with DZ characterised by spatially varying properties. Fig. 5(b, top) shows that the magnitude of P_f is limited in the vicinity of the FC (P_f is of the order of ~25 MPa to be compared to ~30 MPa in case 0) due the spatial distribution of fault-normal permeability within the DZ (Fig. 4a). Consequently, the decrease of the effective stress components $(\sigma_3'; \sigma_1')$ is limited over time as shown by the lateral profiles on Fig. 6. This has an impact on PSF, which is lower than for case 0. Interestingly, Fig. 5(b, bottom) shows that the maximum PSF value is located in DZ in the vicinity of the FC for case 1 (at a distance of about 0.5 m from the FC), whereas it is in the FC for case 0. In the following, we aim at getting better insights in the processes underlying this failure location.

Fig. 7 respectively depicts the stress paths both inside FC and inside the hanging wall's DZ (at a lateral distance of 0.5 m from the FC) at −1515 m depth for cases 0 and 1. Note that the initial stress states are not equal, since the Biot's coefficients are different. In order to judge for the significance of the differences between both cases, we include the lower and upper bound of the stress paths (bounds of the grey-coloured

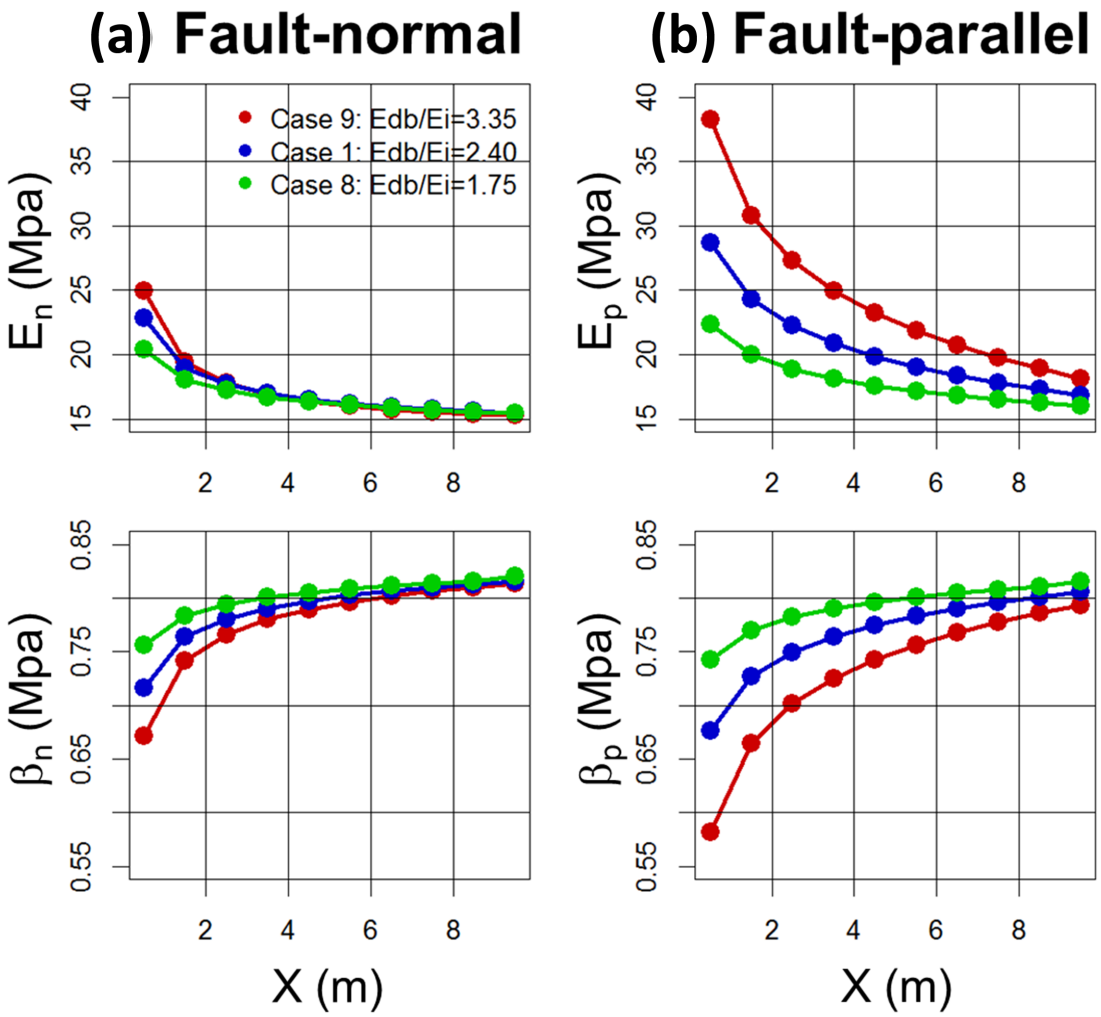

Figure 3. Evolution of the upscaled (effective) poroelastic DZ properties as a function of the lateral distance to the fault core X considering different cases (see Table 2) of Young's modulus contrasts E_{db}/E_i ('i' denotes the intact porous matrix; 'db' denotes the deformation band): (a) fault-normal Young's modulus E_n; (b) fault-parallel Young's modulus E_p; (c) fault-normal Biot's coefficient β_n; (d) fault-parallel Biot's coefficient β_p.

envelope in Fig. 7) related to a typical uncertainty for fault stability analysis, namely the estimate of the initial stress state defined here via K_0 (ratio of the initial horizontal to vertical total stress), which is assumed to range from 0.60 to 0.80.

For case 0 (black lines in Fig. 7), the temporal evolution of the effective stresses is quasi-linear inside FC and DZ with a temporal decrease of σ_3' during injection steeper than for σ_1' in FC compared to DZ (slope of the linear fit of ~0.75 for FC compared to ~1.13 for DZ). The shear failure is first initiated in FC before DZ (considering the failure line defined for $\mu = 0.6$ and $C_0 = 0$). The presence of the spatially varying DZ properties (case 1 outlined by blue lines in Fig. 7) tends to 'break the quasi-linear' temporal stress evolution: σ_1' steeply decreases over time compared to σ_3' in the early stages up to the 4th time step (slope of the linear fit of ~2.72 within DZ); then, the tendency is reversed and σ_3' turns to be the one decreasing the most (slope of the linear fit of ~0.32 within DZ). The influence on the stress paths can be considered significant, since they fall outside the uncertainty envelope related to the initial stress state's parameter K_0.

The shape of the stress paths inside the FC (Fig. 7a) is similar to the ones inside DZ (Fig. 7b), but the temporal evolution of the stresses is 'slower' than the one for case 0 (indicated by the line length linking subsequent dot-like markers): the stress path does not reach the failure line at the end of injection, and remains within the uncertainty envelope related to K_0.

In terms of maximum sustainable pore pressure P_{max} (i.e. the pore pressure for which the stress path reaches the failure line), the afore-described analysis shows that P_{max} is larger for case 1 than for case 0: in this sense, the fault can be said to be 'strengthened'. Conversely, if P_{max} is lower, the system can be said to be 'weakened'.

3.3 Contribution of the different DZ characteristics

To get better insight into the role of different DZ characteristics (complex spatial distribution, anisotropy, Young's modulus versus Biot's coefficients, etc.), a series of parametric studies are conducted (Figs 7–9). The different properties are set in turn to a constant spatially

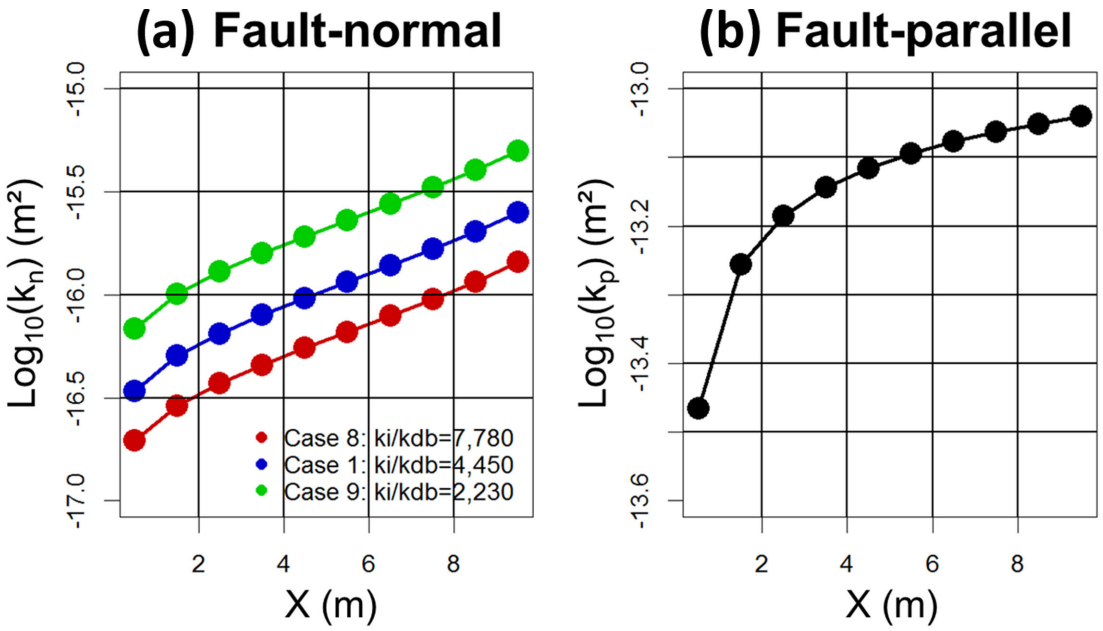

Figure 4. Evolution of the upscaled (effective) permeability of DZ as a function of the lateral distance to the fault core X considering different cases (see Table 2) of permeability contrasts k_i/k_{db} ('i': the intact porous matrix; 'db': the deformation band): (a) fault-normal permeability k_n (logarithm, base 10); (b) fault-parallel permeability k_p.

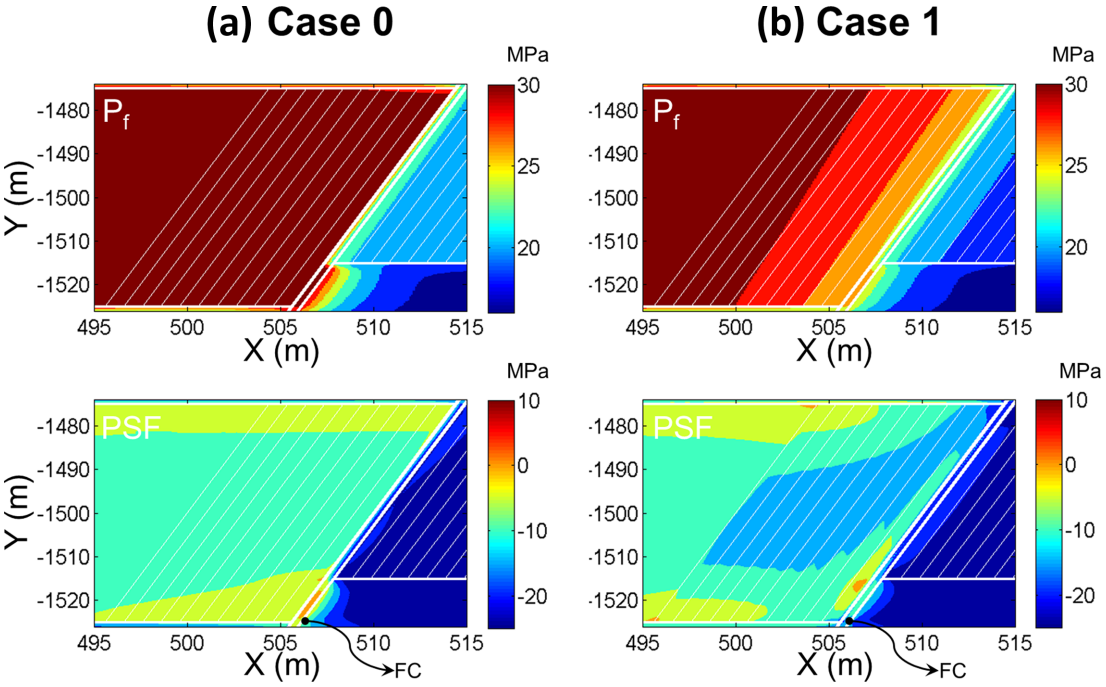

Figure 5. Mapping of the pore pressure P_f (MPa) and of the potential for shear failure (PSF) at the end of injection considering: (a) case 0: a fault zone without any DZ; (b) case 1: a fault zone with a DZ whose spatially varying properties correspond to the ones depicted in blue in Figs 3 and 4 (case 1).

homogeneous value (e.g. case 2 refers to the simulation case where all the properties are spatially varying expect for the fault-normal Young's modulus E_n set to 15 GPa, i.e. to the reservoir Young's modulus). See the summary of the different simulation cases in Table 2.

We first analyse the influence of the Young's modulus (Fig. 7) on the stress paths. Setting $E_p = 15$ GPa (case 3) for DZ has clearly the largest influence on the stress paths within both DZ and FC (red lines in Fig. 7). P_{max} appears to be larger than in case 0: the stress state at the end of injection corresponds to the one for case 0 after six time steps. Thus, the higher the fault-parallel Young's modulus, the higher the shear failure potential. In this case (constant E_p), stress evolution is linear (compared to the bilinear stress evolution in case 1) with steeper slope than for case 0: this indicates that the complex stress changes are primarily driven by the complex spatial distribution of E_p. In contrary, setting the fault-normal Young's modulus $E_n = 15$ GPa (case 2) has very little impact (green lines in Fig. 7) especially with respect to the uncertainty on the estimate of the initial stress state's parameter K_0.

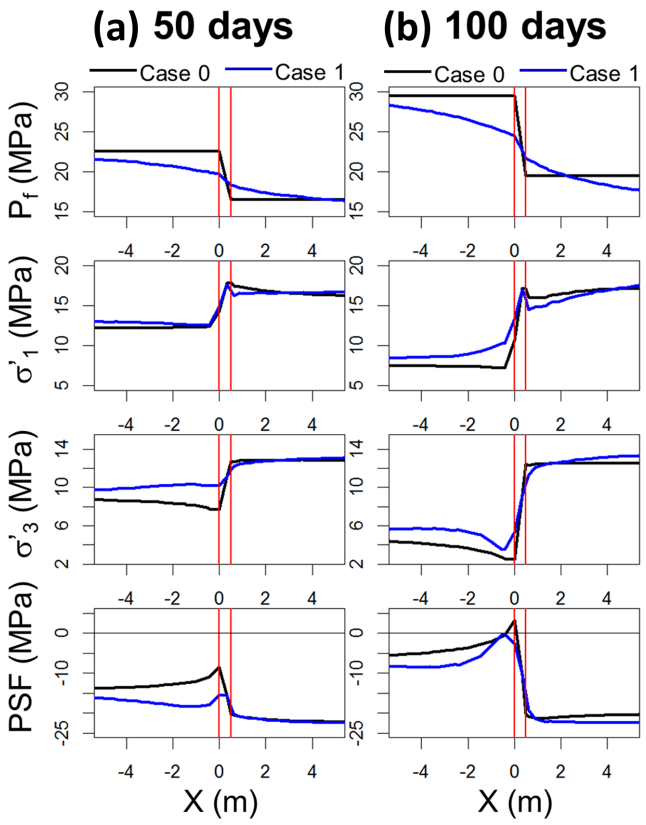

Figure 6. Lateral profile of pore pressure P_f, effective stress components $(\sigma_3'; \sigma_1')$ and the potential for shear failure (PSF; calculated for a friction coefficient $\mu = 0.6$), at -1515-m depth in the vicinity of the fault core FC (indicated by red-coloured vertical lines) after: (a) 50 days of injection; (b) at the end of injection after 100 days. Two cases are considered: case 0 (fault zone without DZ); case 1 (fault zone with DZ characterized by spatially varying properties, see Table 2).

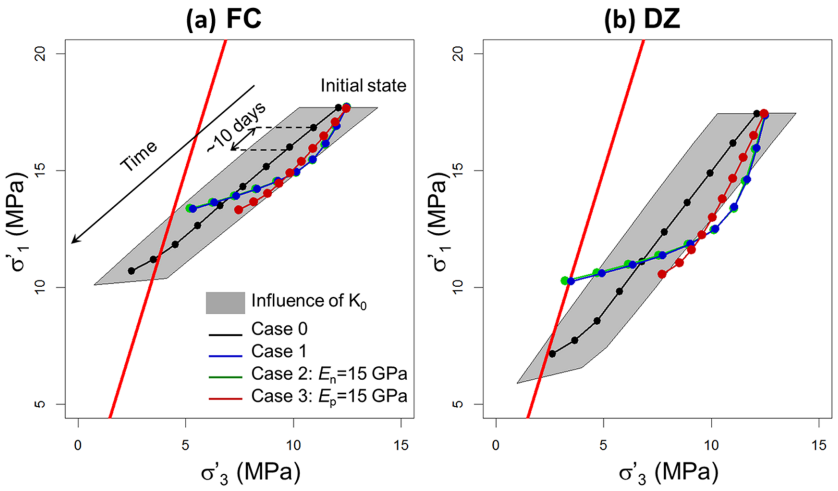

Figure 7. Temporal evolution of stress paths at -1515-m depth in the $(\sigma_3'; \sigma_1')$ domain: (a) within the FC; (b) within the DZ at a lateral distance of 0.5 m from FC. Different cases for the Young's modulus of DZ are considered (see Table 2). Case 2 corresponds to a fault-normal DZ Young's modulus E_n fixed at the reservoir Young's modulus of 15 GPa, whereas case 3 corresponds to a fault-parallel DZ Young's modulus E_p fixed to 15 GPa. The failure line for which $\sigma_1' = 3 \times \sigma_3'$ is indicated in red.

Setting the Biot's coefficients to their maximum value of 1.0 has different consequences (Fig. 8): the higher β_p, the lower P_{max}, but without influencing the curvature of the stress evolution (compare case 5 and case 1 in Figs 8a and b). On the contrary, β_n tends to act on this curvature: the higher β_n, the lower the curvature.

Setting the fault-parallel permeability $k_p = 10^{-17}$ m^2 (core permeability) appears to have a quasi-similar effect as setting $\beta_p = 1.0$ (compare case 5 and case 7 in Figs 8b and 9b), whereas setting it to 10^{-13} m^2 (reservoir permeability) has little effect (not shown). Both properties act on the magnitude of the pore pressure, but in different manners: k_p slows the vertical flow, whereas β_p acts on the magnitude of the hydromechanical coupling (eq. 1). Setting $k_n = 10^{-13}$ m^2 (reservoir permeability) has a similar effect on the curvature of the stress

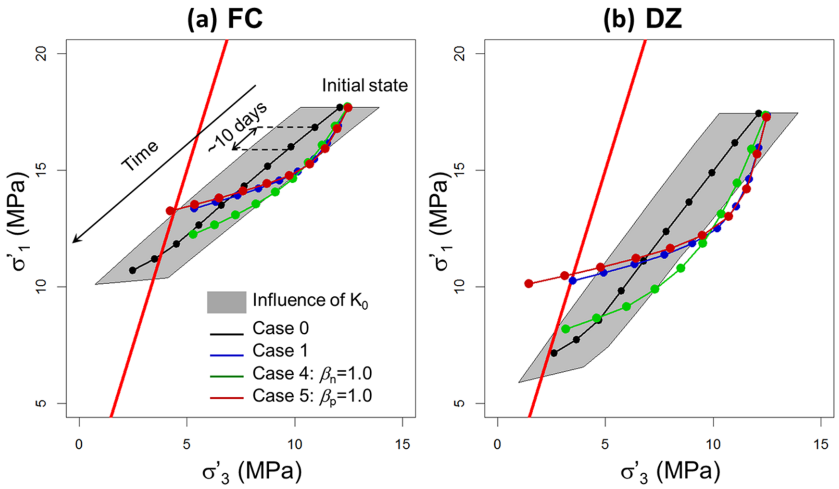

Figure 8. Temporal evolution of stress paths at −1515-m depth in the $(\sigma_3';\sigma_1')$ domain: (a) within the FC; (b) within the DZ at a lateral distance of 0.5 m from FC. Different cases for the Biot's coefficient of DZ are considered (see Table 2). Case 4 corresponds to a fault-normal DZ Biot's coefficient fixed at $\beta_n = 1.0$, whereas case 5 corresponds to a fault-parallel DZ Biot's coefficient fixed to $\beta_p = 1.0$. The failure line for which $\sigma_1' = 3 \times \sigma_3'$ is indicated in red.

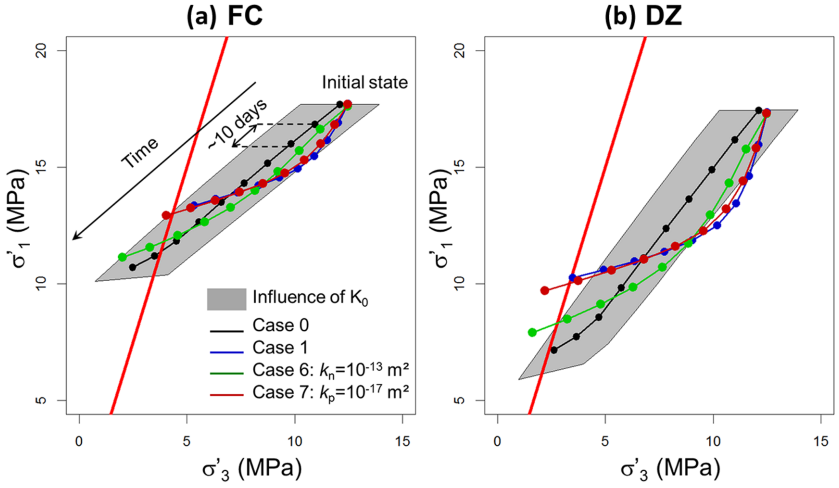

Figure 9. Temporal evolution of stress paths at −1515-m depth in the $(\sigma_3';\sigma_1')$ domain: (a) within the FC; (b) within the DZ at a lateral distance of 0.5 m from FC. Different cases for the DZ permeability are considered (see Table 2). Case 6 corresponds to a fault-normal permeability fixed at $k_n = 10^{-13}$ m^2 (host reservoir permeability), whereas case 7 corresponds to a fault-parallel permeability fixed at $k_p = 10^{-17}$ m^2 (FC permeability). The failure line for which $\sigma_1' = 3 \times \sigma_3'$ is indicated in red.

evolution as setting $\beta_n = 1.0$ (compare case 4 and case 6 in Figs 8b and 9b), but pushes the system towards failure by accelerating the stress evolution between the subsequent time steps: this is related to the enhancement of lateral flow towards the FC. Hence, the fault-normal permeability plays a 'protective' role by hindering the pore pressure increase in the vicinity of the FC, hence limiting the effective stresses' decrease.

3.4 Influence of the properties contrast on failure potential (PSF)

The afore-described failure potential is dependent on the contrast of permeability k_i/k_{db} and on the contrast of Young's modulus E_{db}/E_i. By linearly varying E_{db}/E_i from 1.5 to 3.5 and the permeability contrast k_i/k_{db} from 1000 to 8000, we calculated the relative PSF differences between case 0 and the cases with spatially varying DZ properties (Fig. 10). Several observations can be made:

(1) The potential for shear failure PSF is systematically below the one for case 0 within the FC (note the iso-contour at 0.0 in Fig. 10a). The lower E_{db}/E_i and the higher k_i/k_{db} (top left hand corner of Fig. 10a), the larger the limitation of shear failure.

(2) On the other hand, the shear failure of DZ can be promoted or inhibited depending on the value of E_{db}/E_i and on k_i/k_{db}. For low E_{db}/E_i (below ≈2.25) and high k_i/k_{db} (above ≈2500), the failure is limited (the PSF differences are positive) with largest effect due to E_{db}/E_i (the

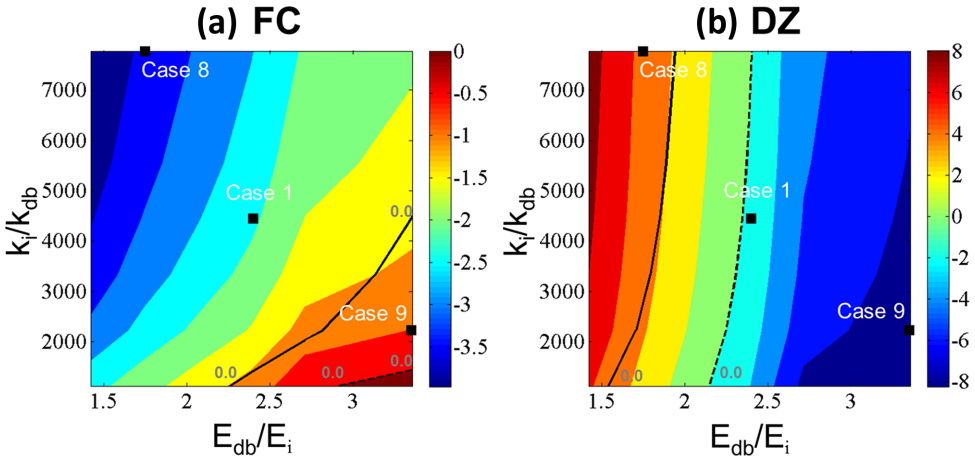

Figure 10. Parameter-space study of the PSF differences (in MPa) at the end of injection at −1515-m depth between case 0 (fault zone without DZ) and cases with DZ spatially varying properties depending on the Young's modulus contrast E_{db}/E_i versus the permeability contrast k_i/k_{db}: (a) within the FC; (b) within DZ at a lateral distance of 0.5 m from FC; the dashed line outlines the iso-contour at 0.0, whereas the solid line outlines the iso-contour at 0.0 but for a parameter space study assuming constant Biot's coefficients at 1.0.

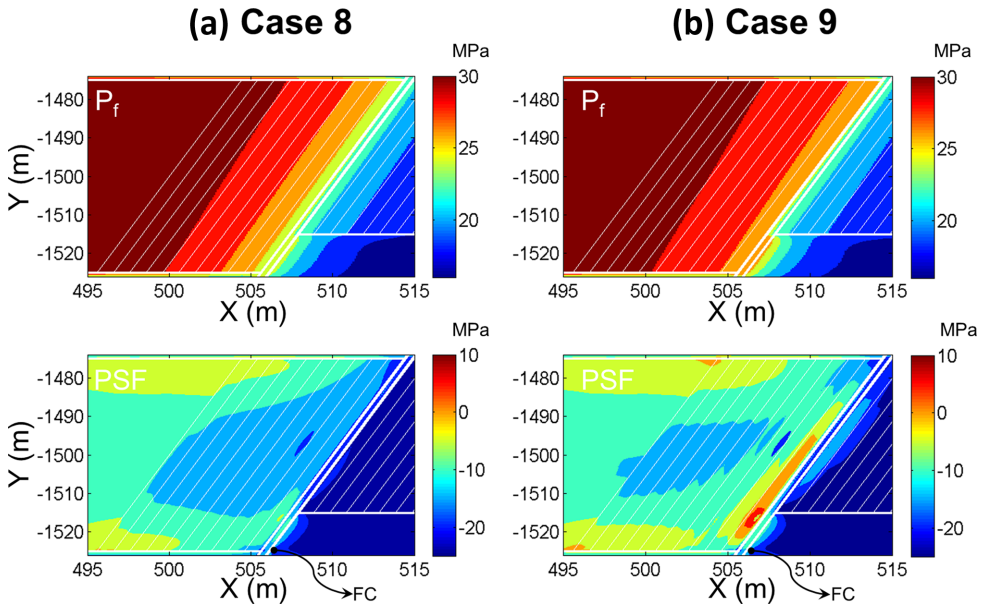

Figure 11. Mapping of the pore pressure P_f (MPa) and of the potential for shear failure (PSF) at the end of injection considering: (a) case 8: a fault zone with low Young's modulus contrast ($E_{db}/E_i = 1.75$) and high-permeability contrast ($k_i/k_{db} = 7780$); (b) case 9: a fault zone with high Young's modulus contrast ($E_{db}/E_i = 3.35$) and low-permeability contrast ($k_i/k_{db} = 2230$).

iso-contours in Fig. 10b are almost vertical) in this region of contrast values. For high E_{db}/E_i (above ≈2.25) shear failure is promoted (the PSF differences are negative) so that the lower k_i/k_{db}, the higher the enhancement of the failure potential (bottom right hand corner of Fig. 10b);

(3) As underlined in Section 3.3, this failure limitation is also related to the effect of the Biot's coefficient: re-conducting the same parameter space study but with Biot's coefficients at 1.0 indicates that the iso-contour for the PSF differences at 0.0 is translated to the left (see position of the black line compared to the dashed one in Fig. 10). This implies that there are contrast's values for which shear failure can be promoted inside the FC.

To further illustrate, Fig. 11 depicts the PSF spatial distribution at the end of injection for two extreme cases, namely case 8 with low Young's modulus contrast and high-permeability contrast: $E_{db}/E_i = 1.75$ and $k_i/k_{db} = 7780$; case 9 with high Young's modulus contrast and moderate permeability contrast: $E_{db}/E_i = 3.35$ and $k_i/k_{db} = 2230$. These cases are also reported in Fig. 10.

The spatial distribution of P_f is almost similar between both cases (Fig. 11, top), but with largest differences in the underburden formation adjacent to the hanging-wall reservoir compartment: the lateral spreading of P_f is more limited for case 8 since the permeability contrast is the larger. The spatial distribution of PSF reveals a maximum value of the order of 10 MPa for case 9, whereas PSF remains negative for

case 8 (shear failure is limited). Interestingly, the spatial extent of the zone for which PSF exceeds zero vertically spreads over more than half of the reservoir thickness (note the orange-coloured region).

4 DISCUSSION AND FURTHER WORKS

The primary emphasis of the present simulation-based study is to improve the knowledge on the injection-induced shear reactivation of reservoir-bounding normal faults characterized by high-stiff/low-permeable DZs. We focus on the presence of cataclastic bands with high stiffness and low permeability, but the study can also be valid for pure compaction bands and veins. The importance of integrating the hydromechanical heterogeneities of DZ in reservoir models for fault stability analysis is demonstrated through numerical simulations: neglecting the DZ might over-estimate the maximum sustainable injection pressure. Analysing these results in the light of a typical source of uncertainty for fault analysis, namely the estimate of the initial stress state, confirms the significance of the influence of the DZ characteristics on the shear behaviour of the studied normal fault. This justifies intensifying in-site geological surveys as reported for instance, by Alikarami *et al.* (2013). The parametric study of Section 4.3 shows that the DB-controlled DZ properties act in different manners and potentially compensate each other. The increase of the fault-parallel Young's modulus alone enhances the decrease of the minimum principal effective stress σ_3' while limiting the decrease of σ_1': this promotes the shear failure (linked with $\sigma_1' - \sigma_3'$). Conversely, the fault-parallel Biot's coefficient, which negatively correlates with the Young's modulus, limits this effect by lowering the magnitude of the hydromechanical coupling. Similarly, the low fault-normal effective permeability prevents the increase of the pore pressure near the fault, hence limits shear reactivation in the FC.

Numerous studies have addressed the question of fault stability by adopting the 'seal-conduit' concept (Fig. 1) as underlined in the introduction. One major concern is the impact of DZ heterogeneities on the flow in the vicinity of the FC (see an example in carbonate setting by Jeanne *et al.* 2013) or on the evolution of deformation of the fault, which could eventually promote shear slip (e.g. Cappa 2011; Rohmer 2014). In the present study, we consider a fault zone's architecture of 'seal-seal' type (with low-permeable FC and DZ, Fig. 1). Intuitively, the risk of integrity loss (decrease of sealing capacity) of such a system is expected to be lower. Recall that the presence of DB implies a decrease of the fault-normal permeability (as low as $1.5e^{-17}$ for high-permeability contrast, Fig. 4a).

Yet, our results showed that this may not be the case depending on the DZ properties (Fig. 10): shear failure potential could be enhanced off-fault, which could potentially lead to the creation of new preferential flow pathways during fluid injection. This process is primarily controlled by the fault-parallel DZ stiffness: higher stiffness contrast promotes off-fault failure. Interestingly, this shear preferential location at low-permeable, high-stiff zones has also been reported by the in-site survey of Guglielmi *et al.* (2008), hence highlighting the importance of material properties' contrasts.

Shear failure is investigated in terms of potential, that is, distance to the cohesion threshold $\hat{C}_0$ as defined in eq. 3. This allows us to span a broad range of situations. In case of late cementation of DB, the DZ can be stronger than the host rock itself so that $\hat{C}_0$ may be high and shear reactivation might not be initiated considering our numerical results. On the contrary, cohesion can be as low as the host rock for alternative situations: 1. poorly cemented (unlithified) sandstones with high degree of cataclasis, which could involve high degree of grain crushing; 2. presence of slip surfaces (i.e. fractures with low cohesion) overprinting DB, as reported for instance on field by Davatzes & Aydin (2003). Besides, recent experimental studies by Torabi & Skurtveit (2013) showed that granulation and grain size reduction could even lead to lower shear modulus in the bands. In those situations, the shear reactivation in the near-zone of the FC is likely to be enhanced as shown by the spatial distribution of PSF in Figs 5(b) and 11(b). In particular, for case 9, PSF reaches large values up to 10 MPa inside the DZ in the vicinity of the FC so that the shear reactivation could be reached even considering non-zero cohesion. To further model the rupture processes after this initiation of shear reactivation, fault slip weakening should be accounted for, for instance by linking plastic shear strain to the coefficient of friction μ and to the induced degradation of hydraulic properties (see further details provided by Cappa 2011). This constitutes a line for future research, since this would also require accounting for an anisotropic poro-plastic rheology (e.g. Chen *et al.* 2010).

Though our numerical investigations can be considered as first-order estimates, they can be useful to discuss the consequences of this preferential off-fault damage from a seismicity perspective. In the present study, we assume a 'strong' fault in the sense that both FC and DZ encompass a high friction coefficient of 0.6. The main shock induced by the increase of fluid is expected to be located first within the DZ at the interface with or close to the FC and the main slip surface, and then inside the FC (see for instance the stress evolution in Fig. 6). This behaviour promotes off-fault aftershocks potentially of high energy: the area for which PSF >0.0 in Fig. 11(b) provides an estimate of the potential ruptured zone, which almost reaches half of the reservoir thickness. This behaviour can even be worsened by dynamic rupture: for instance, Ben-Zion & Shi (2005) showed that plastic strain is primarily generated on the stiffer side of the fault zone and the DZ. Conversely, assuming a weak fault (i.e. FC composed of weak material of low coefficient of friction), the main shock is expected to be located first within the limited volume of the FC, then should affect the lateral rock volume outside FC.

Finally, we acknowledge that accounting for only a single fault-parallel DB family (synthetic set) is a simplified vision. Integrating multiple DB families (antithetic sets, or even oblique, see e.g. Jourde *et al.* 2002), which are usually observed in the DZ of natural faults, is a line of future research work. Assessing the shear behaviour in this case is not straightforward: effective permeability is expected to decrease (hence limiting the increase of pore pressure), whereas the stiffness is expected to increase (hence weakening the system). Furthermore, we did not account for the clustering phenomenon (see e.g. Kolyukhin *et al.* 2010 for DB and Roy *et al.* 2014 for fractures). The numerical investigations reported here could be extended in the future by relying, for instance, on more advanced numerical upscaling techniques like the one developed for fractured porous media (Min & Jing 2003).

ACKNOWLEDGEMENTS

The research leading to these results has been carried out in the framework of the ULTIMATE-CO_2 Project, funded by the European Commission's Seventh Framework Program [FP7/2007–2013] under grant agreement no. 281196. AT is grateful to the Centre for Integrated Petroleum Research (CIPR) at Uni Research and the Research Council of Norway. We thank both reviewers for their constructive comments, which led to the improvement of the manuscript.

REFERENCES

Alikarami, R., Torabi, A., Kolyukhin, D. & Skurtveit, E., 2013. Geostatistical relationships between mechanical and petrophysical properties of deformed sandstone, *Int. J. Rock Mech. Min. Sci.*, **63**, 27–38.

Ben-Zion, Y. & Shi, Z., 2005. Dynamic rupture on a material interface with spontaneous generation of plastic strain in the bulk, *Earth planet. Sci. Lett.*, **236**, 486–496.

Biot, M.A., 1941. General theory of three-dimensional consolidation, *J. Appl. Phys.*, **12**, 155–164.

Caine, J.S., Evans, J.P. & Forster, C.B., 1996. Fault zone architecture and permeability structure, *Geology*, **24**, 1025–1028.

Cappa, F., 2011. Influence of hydromechanical heterogeneities of fault zones on earthquake ruptures, *Geophys. J. Int.*, **185**, 1049–1058.

Cappa, F. & Rutqvist, J., 2011. Impact of CO_2 geological sequestration on the nucleation of earthquakes, *Geophys. Res. Lett.*, **38**, L17313, doi:10.1029/2011GL048487.

Carroll, M., 1979. An effective stress law for anisotropic elastic deformation, *J. geophys. Res.*, **84**, 7510–7512.

Chen, L., Shao, J.F. & Huang, H.W., 2010. Coupled elastoplastic damage modeling of anisotropic rocks, *Comput. Geotech.*, **37**(1), 187–194.

Chen, Q. & Nur, A., 1992. Pore fluid pressure effects in anisotropic rocks: mechanisms of induced seismicity and weak faults, *Pure appl. Geophys.*, **139**, 463–479.

Coussy, O., 2004. *Poromechanics*, John Wiley & Sons, Ltd.

Davatzes, N.C. & Aydin, A., 2003. Overprinting faulting mechanisms in high porosity sandstones of SE Utah, *J. Struct. Geol.*, **25**(11), 1795–1813.

Dunham, E.M. & Rice, J.R., 2008. Earthquake slip between dissimilar poroelastic materials, *J. geophys. Res.*, **113**, B09304, doi:10.1029/2007JB00540.

EDF R&D, 2012. Code_Aster, Analysis of Structures and Thermomechanics for Studies & Research, description on numerical implementation of thermo-hydraumechanical processes, Available at: http://www.code-aster.org/V2/doc/default/en/man_r/r7/r7.01.10.pdf, last accessed 22 June 2015.

Ellsworth, W., 2013. Injection-induced earthquakes, *Science*, **341**, 142–149.

Faulkner, D.R., Jackson, C.A.L., Lunn, R.J., Schlische, R.W., Shipton, Z.K., Wibberley, C.A.J. & Withjack, M.O., 2010. A review of recent developments concerning the structure, mechanics and fluid flow properties of fault zones, *J. Struct. Geol.*, **32**, 1557–1575.

Faulkner, D.R., Mitchell, T.M., Healy, D. & Heap, M.J., 2006. Slip on 'weak' faults by the rotation of regional stress in the fracture damage zone, *Nature*, **444**, 922–925.

Fisher, Q.J. & Knipe, R.J., 2001. The permeability of faults within siliciclastic petroleum reservoirs of the North Sea and Norwegian Continental Shelf, *Mar. Pet. Geol.*, **18**, 1063–1081.

Fossen, H., Schultz, R.A., Shipton, Z.K. & Mair, K., 2007. Deformation bands in sandstone: a review, *J. geol. Soc. Lond.*, **164**, 755–769.

Guglielmi, Y., Cappa, F. & Amitrano, D., 2008. High-definition analysis of fluid-induced seismicity related to the mesoscale hydromechanical properties of a fault zone, *Geophys. Res. Lett.*, **35**, L06306, doi:10.1029/2007GL033087.

Hawkes, C.D., McLellan, P.J., Zimmer, U. & Bachu, S., 2004. Geomechanical factors affecting geological storage of CO_2 in depleted oil and gas reservoirs: risks and mechanisms, in *Proceedings of Gulf Rocks 2004, the 6th North America Rock Mechanics Symposium (NARMS): Rock Mechanics Across Borders and Disciplines*, Houston, TX, USA.

Jaeger, J.C. & Cook, N.G.W., 1979. *Fundamentals of Rock Mechanics*, 3rd edn, Chapman & Hall.

Jeanne, P., Guglielmi, Y. & Cappa, F., 2013. Dissimilar properties within a carbonate-reservoir's small fault zone, and their impact on the pressurization and leakage associated with CO_2 injection, *J. Struct. Geol.*, **47**, 25–35.

Jeanne, P., Guglielmi, Y., Cappa, F., Rinaldi, A.P. & Rutqvist, J., 2014. The effects of lateral property variations on fault-zone reactivation by fluid pressurization: application to CO_2 pressurization effects within major and undetected fault zones, *J. Struct. Geol.*, **62**, 97–108.

Jourde, H., Flodin, E.A., Aydin, A., Durlofsky, L.J. & Wen, X.H., 2002. Computing permeability of fault zones in eolian sandstone from outcrop measurements, *AAPG Bull.*, **86**(7), 1187–1200.

Kaproth, B.M., Cashman, S.M. & Marone, C., 2010. Deformation band formation and strength evolution in unlithified sand: the role of grain breakage, *J. geophys. Res.*, **115**(B12), doi:10.1029/2010JB007406.

Kolyukhin, D., Schueller, S., Espedal, M. & Fossen, H., 2010. Deformation band populations in fault damage zone—impact on fluid flow, *Computational Geoscience*, **14**, 231–248.

Kolyukhin, D. & Torabi, A., 2012. Statistical analysis of the relationships between faults attributes, *J. geophys. Res.*, **117**, B05406, doi:10.1029/2011JB008880.

Mair, K., Main, I. & Elphick, S., 2000. Sequential growth of deformation bands in the laboratory, *J. Struct. Geol.*, **22**(1), 25–42.

Manzocchi, T., Childs, C. & Walsh, J.J., 2010. Faults and fault properties in hydrocarbon flow models, *Geofluids*, **10**(1–2), 94–113.

Markov, K.Z., 1999. Elementary micromechanics of heterogeneous media, in *Heterogeneous Media: Modeling and Simulation*, eds Markov, K.Z. & Preziosi, L., Birkhauser.

Matonti, C., Lamarche, J., Guglielmi, Y. & Marié, L., 2012. Structural and petrophysical characterization of mixed conduit/seal fault zones in carbonates: example from the Castellas fault (SE France), *J. Struct. Geol.*, **39**, 103–121.

Mazzoldi, A., Rinaldi, A.P., Borgia, A. & Rutqvist, J., 2012. Induced seismicity within geological carbon sequestration projects: maximum earthquake magnitude and leakage potential from undetected faults, *Int. J. Greenhouse Gas Control*, **10**, 434–442.

Min, K.B. & Jing, L., 2003. Numerical determination of the equivalent elastic compliance tensor for fractured rock masses using the distinct element method, *Int. J. Rock Mech. Min. Sci.*, **40**(6), 795–816.

Petrie, E.S., Petrie, R.A. & Evans, J.P., 2014. Identification of reactivation and increased permeability associated with a fault damage zone using a multidisciplinary approach, *J. Struct. Geol.*, **59**, 37–49.

Rohmer, J., 2014. Induced seismicity of a normal blind undetected reservoir-bounding fault influenced by dissymmetric fractured damage zones, *Geophys. J. Int.*, **197**, 636–641.

Roy, A., Perfect, E., Dunne, W.M. & McKay, L.D., 2014. A technique for revealing scale-dependent patterns in fracture spacing data, *J. geophys. Res.*, **119**, 5979–5986.

Rudnicki, J.W. & Rice, J.R., 2006. Effective normal stress alteration due to pore pressure changes induced by dynamic slip propagation on a plane between dissimilar materials, *J. geophys. Res.*, **111**, B10308, doi:10.1029/2006JB004396.

Schueller, S., Braathen, A., Fossen, H. & Tveranger, J., 2013. Spatial distribution of deformation bands in damage zones of extensional faults in porous sandstones: statistical analysis of field data, *J. Struct. Geol.*, **52**, 148–162.

Schultz, R. & Siddharthan, R., 2005. A general framework for the occurrence and faulting of deformation bands in porous granular rocks, *Tectonophysics*, **411**, 1–18.

Shimamoto, T. & Logan, J.M., 1981. Effects of simulated clay gouges on the sliding behavior of Tennessee sandston, *Tectonophysics*, **75**(3), 243–255.

Shipton, Z.K. & Cowie, P.A., 2001. Damage zone and slip-surface evolution over [mu]m to km scales in high-porosity Navajo sandstone, Utah, *J. Struct. Geol.*, **23**(12), 1825–1844.

Tondi, E., Antonellini, M., Aydin, A., Marchegiani, L. & Cello, G., 2006. The role of deformation bands, stylolites and sheared stylolites in fault development in carbonate grainstones of Majella Mountain, Italy, *J. Struct. Geol.*, **28**, 376–391.

Torabi, A. & Alikarami, R., 2012. Heterogeneity within deformation bands in sandstone reservoirs. in *American Rock Mechanics Association (ARMA), in 46th US Rock Mechanics/Geomechanics Symposium*, Chicago, IL, USA.

Torabi, A. & Skurtveit, E., 2013. Effect of initial grain size and packing on the evolution of elastic properties of poorly lithified sandstones, in *American Rock Mechanics Association (ARMA), 47th US Rock Mechanics/Geomechanics Symposium*, San Francisco, CA, USA.

Torabi, A. & Zarifi, Z., 2014. Energy release rate of propagating deformation bands and their hosted cracks, *Int. J. Rock Mech. Min. Eng.*, **67**, 184–190.

Underhill, J.R. & Woodcock, N.H., 1987. *Faulting Mechanisms in High-porosity Sandstones, New Red Sandstone, Arran, Scotland*, Vol. 29, pp. 91–105, Geological Society, Special Publications.

USEPA (U.S. Environmental Protection Agency), 1994. *Determination of Maximum Injection Pressure for Class I Wells*, United States Environmental Protection Agency.

Viesca, R.C., Templeton, E.L. & Rice, J.R., 2008. Off-fault plasticity and earthquake rupture dynamics: 2. Effects of fluid saturation, *J. geophys. Res.*, **113**, B09307, doi:10.1029/2007JB005530.

Wibberley, C.A.J., Yielding, G. & Di Toro, G., 2008. *Recent Advances in the Understanding of Fault Zone Internal Structure: A Review*, Vol. 299, pp. 5–33, Geological Society, Special Publication.

Yielding, G., Freeman, B. & Needham, D.T., 1997. Quantitative fault seal prediction, *AAPG Bull.*, **81**, 897–917.

Zhao, Y.H. & Weng, G.J., 1990. Effective elastic moduli of ribbon-reinforced composites, *J. appl. Mech.*, **57**(1), 158–167.

Zoback, M.D. & Gorelick, S.M., 2012. Earthquake triggering and largescale geologic storage of carbon dioxide, *Proc. Natl. Acad. Sci. U.S.A.*, doi:10.1073/pnas.1202473109.

APPENDIX: GOVERNING EQUATIONS OF THE PORO-ELASTIC BEHAVIOUR

In this appendix, we briefly introduce the main equations governing the fully saturated isothermal orthotropic poro-elastic behaviour of the rock materials. Full details can be found for instance in Biot (1941) and Coussy (2004).

The effective stress tensor $\boldsymbol{\sigma}'$ is linked to the deformation $\boldsymbol{\varepsilon}$ and the pore pressure P_f by

$$d\boldsymbol{\sigma}' = \boldsymbol{C} : d\boldsymbol{\varepsilon} - \beta d P_f, \tag{A1}$$

where $\boldsymbol{C}$ is the stiffness tensor of drained matrix, which is fully specified via nine coefficients assuming an orthotropic elastic material (in 3-D) as follows:

$$\boldsymbol{C} = \begin{pmatrix} c_{11} & c_{12} & c_{13} & & & \\ c_{12} & c_{22} & c_{23} & & & \\ c_{13} & c_{23} & c_{33} & & & \\ & & & c_{44} & & \\ & & & & c_{55} & \\ & & & & & c_{66} \end{pmatrix}. \tag{A2}$$

The Biot's tensor $\boldsymbol{\beta}$ is given by:

$$\boldsymbol{\beta} = \boldsymbol{C}{:}\boldsymbol{\beta}^* \text{ with } \boldsymbol{\beta}^* = (\boldsymbol{S} - \boldsymbol{S}^S) : \boldsymbol{\delta} \tag{A3}$$

with $\boldsymbol{\delta} = \delta_{kl} e_k \otimes e_l$ with Kronecker delta $\delta_{kl} = 1$ if $k = \mathrm{l}$, 0 otherwise.

$\boldsymbol{S}^\mathrm{S}$ and $\boldsymbol{S}$ are the compliance tensors of the solid and the drained matrix, respectively. The former tensor is linked to the Young's modulus and Poisson's ratio of the solid matrix, which are assumed to be isotropic and homogeneous in the present study.

The pore pressure gradient is assumed to be linked to the mass flow $\boldsymbol{M}_\mathrm{f}$ by the Darcy's law as follows:

$$\frac{\boldsymbol{M}_\mathrm{f}}{\rho_\mathrm{f}} = \frac{\boldsymbol{k}}{\mu_\mathrm{f}} \left(-\nabla P_\mathrm{f} + \rho_\mathrm{f} \boldsymbol{g}\right), \tag{A4}$$

where μ_f is the fluid dynamic viscosity, ρ_f is the fluid density, $\boldsymbol{g}$ is the gravity and $\boldsymbol{k}$ is the permeability tensor.

The mass conservation is given by

$$\frac{\partial}{\partial t}\left(m_\mathrm{f}\right) + \mathbf{Div}\left(\boldsymbol{M}_\mathrm{f}\right) = 0, \tag{A5}$$

where the increment of mass of fluid m_f is given by

$$dm_\mathrm{f} = d\omega\rho_\mathrm{f}(1+\varepsilon_\mathrm{V}) + \omega d\rho_\mathrm{f}(1+\varepsilon_\mathrm{V}) + \rho_\mathrm{f}\omega d\varepsilon_\mathrm{V} \tag{A6}$$

where the porosity Eulerian ω is the ratio of the volume of the connected porous space to the actual total volume of the porous medium and is linked to volumetric strain ε_{V} and the pore pressure P_{f} by

$$d\omega = \boldsymbol{\beta} : d\boldsymbol{\varepsilon} - \omega . d\varepsilon_{\mathrm{V}} + \frac{dP_{\mathrm{f}}}{M^{S}}, \tag{A7}$$

where the Biot's modulus M^{S} of the solid matrix is given by:

$$\frac{1}{M^{S}} = (\boldsymbol{\beta} - \omega\boldsymbol{\delta}) : \boldsymbol{S}^{S} : \boldsymbol{\delta}. \tag{A8}$$

Finally, the change in fluid density is related to pore pressure changes as

$$\frac{d\rho_{\mathrm{f}}}{\rho_{\mathrm{f}}} = \frac{dP_{\mathrm{f}}}{K_{\mathrm{f}}}, \tag{A9}$$

where K_{f} is the fluid bulk modulus.